Improving the Magic constant - data-based calibration of phased array radars

Theresa Rexer[1], Björn Gustavsson[1], Juha Vierinen[1], Andres Spicher[1], Devin Ray Huyghebaert[1,4], Andreas Kvammen[1], Robert Gillies[3], and Asti Bhatt[2]

[1]Department of Physics and Technology, UIT the Arctic University of Norway, Tromsø, Norway
[2]SRI, San Francisco, USA
[3]Department of Physics and Astronomy, University of Calgary, Calgary, Alberta, Canada
[4]Department of Physics and Engineering Physics, University of Saskatchewan, Saskatoon, Canada

Correspondence: Theresa Rexer (theresa.rexer@uit.no)

Abstract. We present two methods for improved calibration of multi-point electron density measurements from incoherent scatter radars (ISR). They are based on the well-established Flatfield correction method used in imaging and photography, where we exploit the analogy between independent measurements in separate pixels in one image sensor and multi-beam radar measurements. Applying these correction methods adds to the current efforts of estimating the *magic constant* or *system constant* made for the calibration of multi-point radars, increasing data quality and usability by correcting for variable, unaccounted, and unpredictable variations in system gain. This second-level calibration is especially valuable for studies of plasma patches, irregularities, turbulence, and other research where inter-beam changes and fluctuations of electron density are of interest. The methods are strictly based on electron density data measured by the individual radar and require no external input. This is of particular interest when independent measurements of electron densities for calibration are available only in one pointing direction or not at all. A correction factor is estimated in both methods, which is subsequently used to scale the electron density measurements of a multi-beam ISR experiment run on a phased array radar such as RISR-N, RISR-C, PFISR, or the future EISCAT3D radar. This procedure could improve overall data quality if used as part of the data-processing chain for multi-beam ISRs, both for existing data and for future experiments on new multi-beam radars.

1 Introduction

The polar ionosphere is highly dynamic and contains plasma structures at a large range of scales (e.g. Kintner and Seyler, 1985; Tsunoda, 1988; Tsinober, 2009). Measuring and observing the plasma, the structuring, and their spatiotemporal evolution is necessary to understand the underlying physics. It is thus connected to the larger context of how the ionosphere is coupled to the magnetosphere and the interplanetary space around us. One of the most powerful ground-based instruments to study ionospheric plasma are incoherent scatter radars (ISRs). Currently, there are six ISRs operational and one in construction (at the time of writing) in the high-latitude region in the northern hemisphere. Three of these are dish radars located in the northern Fennoscandia region and on Svalbard, and three are phased array radars located in Resolute Bay, Canada (Bahcivan et al., 2010; Gillies et al., 2016), and Poker Flat, Alaska in North America (Kelly and Heinselman, 2009). The new, state of

the art, phased array European Incoherent Scatter Radar 3D (EISCAT 3D) is currently under construction in Northern Norway (McCrea et al., 2015). In contrast to dish radars, phased array radars are capable of volumetric measurements in multiple

25 directions simultaneously (see for example Lamarche and Makarevich, 2017; Semeter et al., 2009, and references therein). This capability has proved itself to be a powerful tool for studying ionospheric structures such as polar cap patches and density "irregularities" (e.g. Goodwin and Perry, 2022; Lamarche et al., 2020; Forsythe and Makarevich, 2018). Electronic beam steering is used to achieve multiple beams covering the desired field of view and the temporal resolution is limited only by the time needed to achieve an acceptable signal-to-noise ratio in each beam. Depending on the given radar system, many factors

30 affect the quality of the signal, and careful calibrations are needed for any radar.

1.1 Calibration of phased array ISR data

ISRs transmit and receive radio waves that scatter from plasma in the terrestrial ionosphere. The power spectrum of the scattered radar signal is directly proportional to the thermal electron density fluctuations and plasma parameters can then be inferred from the observed waves and fluctuations (see for example Evans, 1969; Fejer and Kelley, 1980, and references therein). Various

35 factors within a given radar system will affect these measurements and their Signal-to-Noise ratio. Consequently, calculations of the plasma parameters and any absolute measurement require calibration. To make a measurement of the absolute electron density with any ISR an independent measurement is required. In many cases, the radar itself can make a measurement of the backscatter from Langmuir waves, the so-called plasmaline, providing a direct measurement of the plasma frequency and thus the electron density (e.g. Bahcivan et al., 2010; Rexer et al., 2018, section 3). For RISR-N and RISR-C of the Advanced

40 Modular Incoherent Scatter Radars (AMISR), located far north in Resolute Bay, Canada, the independent measurement of electron density is particularly challenging as the weak photoelectron fluxes in the polar cap make plasma line measurements difficult. Independent measurements of the electron density for one pointing direction can also be obtained from an ionosonde (Themens et al., 2014). An ionosonde consists of an antenna and a nearby receiver that transmit and receive pulsed radio waves that are swept through the typical ionospheric plasma frequency range (0.5 MHz – 20 MHz) (see for example Baumjohann

45 and Treumann, 2012; Bibl, 1998). Vertically transmitted radio waves are reflected when the transmitted frequency is equal to that of the local plasma frequency, and from the time delay of the reflected signal, the altitude of reflection of the transmitted frequency can be determined. As the plasma frequency is directly related to the plasma density, we can calculate an altitude profile of the electron density on the bottom side of the ionosphere. The measured electron density from the ISR can then be scaled to match that of the ionosonde for that pointing direction. A challenge with ionosonde measurements is that this

50 provides an independent measurement only for one general direction and only for the bottomside ionosphere. Additionally, the direction of the source of the signal in the ionosonde can be somewhat ambiguous resulting in an uncertainty of the actual receive direction of the signal and thus which radar beam and pointing direction to scale.

This issue is more complex when the radar to be calibrated has multiple beams. The power of the received signal, and thus the

55 electron density measurements, are dependent on the two-way gain of the antenna in the direction in which it is transmitted and received. For a phased array radar, the antenna gain is maximized in one pointing direction. All beams pointing in another

direction will have a different gain, which can be determined from the antenna gain pattern (radiation pattern) if known. With the antenna gain pattern, it is then possible to calculate a scaling factor for measurements for all beams off the center of the main antenna lobe.

60

In the AMISR radars, the antenna gain is maximized at bore-sight (Gillies et al., 2018). The antenna gain pattern is modeled, and with an independent measurement of the electron density, a scaling factor is estimated for all beams (Lamarche, 2022). In the AMISR data products, this scaling factor is given as the "system constant" or *ksys*. For the EISCAT radars this constant is called the *Magic constant*. However, even after the most meticulous technical calibration of a multi-beam radar, estimating

65 this constant is difficult as the system gain and antenna pattern change with time. For example, an AMISR radar or the future EISCAT 3D radar might have some antenna elements fail, or parts of the array might be covered in snow and ice affecting the radiation pattern locally. Additionally, the antenna gain pattern may vary greatly with experiment, operating temperature, aging antenna components, ground conditions, etc. These changes can affect the total system gain and ideally, this should be taken into account for every experiment separately.

70

1.2 Flatfield calibration in imaging vs multi-beam radars

Flat field correction is a well-established method that has been developed and applied in imaging and image processing for decades (see e.g. Montgomery et al., 1988; Burke, 1996; Oswalt and Bond, 2013, and references therein). It addresses two problems. The first is that different pixels in a sensor can have their own zero-point, that is, the minimum value on each pixel

75 might be different due to thermal noise, material effects, or electronic effects in the system. In imaging, this is referred to as dark-signal non-uniformity. The second is that different pixels in a single sensor might have a different response (or gain) to the same level of illumination or input. This is referred to as spatial photo response non-uniformity in image sensors (see for example Burke, 1996, Chapter 5). When not accounted for, non-uniformities of a sensor result in false spatial patterns in the image.

80   The correction for the dark signal non-uniformity can be relatively straightforward in imaging and is done by subtracting a Darkfield image or bias frame. The Darkfield image is found by averaging (to reduce noise effects) over many individual images taken with the system at "operating temperature", without exposing the sensor to light (e.g. keeping the lens cover on, not opening the shutter). Thus no illumination can affect the sensor, and the resulting "image" contains only the Darkfield image with its non-uniformities and internal effects of the system.

85   The variation in gain between pixels is traditionally corrected for by a normalization, using Flatfield images (e.g. Burke, 1996). Flatfield images are obtained by taking an image of a flat field, that is, an optically flat or uniform source of light. In Astronomy, the twilight sky is often used (e.g. Oswalt and Bond, 2013). Averaging of a number of Flatfield images gives the mean Flatfield image for the system setup. Ideally, this is done with the same system settings as for the experimental measurements and ensures that any variations in gain between pixels, also between experiments or system setups, are accounted

90 for. The corrected image intensity at pxiel (u, v) are then be calculated as:

$$I_{corr}(u,v) = \Big(I_{raw}(u,v) - I_{Df}(u,v) \Big) G(u,v) \tag{1}$$

$$G(u,v) = \frac{\overline{I_{Ff}} - \overline{I_{Df}}}{I_{Ff}(u,v) - I_{Df}(u,v)} \tag{2}$$

where $I_{corr}(u,v)$ is the corrected image, $I_{raw}(u,v)$ is the raw, uncorrected image and the Darkfield and Flatfield images are

95 indicated I_{Df} and I_{Ff}, respectively. Horizontal bars indicate the mean value over the respective image.

Phased array incoherent scatter radars and cameras are very different instruments designed for different measurements. However, they share a key aspect that allows us to adapt this method traditionally used in imaging, to phased array ISR data analyses. Both attempt to measure their respective parameters over an area in space, using multiple detectors simultaneously.

100 For cameras, a commonly used detector is the charged-coupled device (CCD), an area detector that is capable of measuring many points simultaneously in its field of view. A single modern CCD can commonly capture over 1000 x 1000 pixels (one megapixel) for one image. The multiple radar beams can be seen as the phased array radar analog of image pixels for our purpose. While modern phased array radars do not measure one million beams simultaneously, depending on the given radar mode, they can measure many tens of beams. Thus, the underlying principle of simultaneous, multi-point measurements is

105 analogous in the two fields.

To adapt the Flatfield method to ISR measurements we need to consider the properties of the measurements and how they are made. When estimating electron density using Thomson scatter (Evans, 1969), the ion-line power is related to electron density, N_e, and the ratio of electron and ion temperatures, T_e/T_i, as well as distance and transmit power P_{TX}. The radar antenna diffraction pattern, as well as any constant multiplicative factor errors, are represented with a magic constant, $\triangle$ (*ksys*

110 for AMISR). There can also be a bias in the estimate of the power of the ionospheric return. This may be introduced ~~e.g.,~~ by constraining power estimates to be positively valued, due to radio interference, or by leakage of non-ionospheric system noise via a finite-length receiver impulse response. This bias in echo power is denoted with η. The equation for received power is thus:

$$P_{\text{RX}} + \eta = \frac{\triangle N_e P_{\text{TX}}}{R^2 (1 + \frac{T_e}{T_i})} \tag{3}$$

115 When estimating electron density, the ratio T_e/T_i is determined purely from the shape of the autocorrelation function (or spectrum) of the scattered complex voltage, allowing the electron density to be estimated as follows:

$$\hat{N}_e = (P_{\text{RX}} + \eta) \left(1 + \frac{T_e}{T_i} \right) R^2 P_{\text{TX}}^{-1} \triangle^{-1} G \tag{4}$$

If the magic constant contains an error, this will result in a multiplicative factor error modeled with G in estimated electron densities. G is not to be confused with the antenna gain which often uses the same symbol. Note that the above equation

120   is exactly the same form as Equation 1, with $I_{\mathrm{raw}} = P_{\mathrm{RX}}(1 + T_e/T_i)R^2 P_{\mathrm{TX}}^{-1} \triangle^{-1}$ and $I_{\mathrm{Df}} = \eta P_{\mathrm{RX}}(1 + T_e/T_i)R^2 P_{\mathrm{TX}}^{-1} \triangle^{-1}$.
Calculating G correctly will thus improve the electron density measurements.

In this paper, we present two calibration methods. In essence, both are the same general method in that an attempt is made
to estimate a correction factor G that is subsequently used to scale the electron density data in the same form as in Equation
125   1 and 4. They differ in the method in which the correction factor is acquired. The first is based on a well-known technique
from imaging and photography. The second is derived from the distribution of an electron density ratio inferred from the
measurements. Both methods only require the electron density data from a multi-point radar experiment, and no external
measurements are necessary. The methods and calculations are shown in section 2. In anticipation of the EISCAT 3D radar
(McCrea et al., 2015; Kero et al., 2019), we utilize data from the AMISR phased array radar system to investigate the calibration
130   techniques described here in three examples for different experiments and seasons. These are shown in Section 3. A quality
and error estimate calculation is presented in Section 4 and Section 5 will provide a discussion, and suggestions for future
multi-point radar measurements. Section 6 summarizes our conclusions.

2   Method

2.1   Flatfield correction of multi-point ISR data

135   In image processing the Flatfield corrected image can be obtained using Equation 1, with a Flatfield image, and a Darkfield
image. For a phased array radar, there is no lens cover or equivalent way to make a Darkfield measurement. In a similar manner,
it is not easy to get a true Flatfield measurement for a phased array radar as there is nothing similar to a "known" uniform or
blank area of the ionosphere to look at. However, we can make an approximation of the Flatfield measurement in some cases.
A quiet time period in the electron density data of all beams of a given experiment, where no patches, precipitation, or other
140   plasma disturbances or irregularities can be identified, might be used for this. We can adapt Equation 1 for electron density
N_e by considering every horizontal altitude slice through all beams, as an "image" of the electron density. Calculating for one
altitude at a time, the mean of the electron density over the identified quiet time period in beam i, gives the Flatfield density,
$N_e^{Ff}(i)$, for that beam. The Flatfield density image, N_e^{Ff}, for the given altitude, is then constructed from $N_e^{Ff}(i)$ of all beams.
Thus we can get an expression for the corrected electron density, N_e^{corr}, in all beams at one altitude, for multi-point radar
145   measurements as:

$$N_e^{corr} = (N_e^{org} - N_e^{Df})G_{FFC}$$

$$G_{FFC} = \frac{\overline{N_e^{Ff}} - \overline{N_e^{Df}}}{N_e^{Ff} - N_e^{Df}} \tag{5}$$

where N_e^{Df} is the electron density Darkfield, N_e^{Ff} is the electron density Flatfield, N_e^{org} is the uncorrected electron density measurement, and G_{FFC} is the calculated correction factor for this Flatfield correction. Horizontal bars indicate the mean for the respective value. An example of a time period with ISR measurements suitable as a Flatfield density is shown in Figure

150 1. This example is from the RISR-N and RISR-C radars in Resolute Bay, Canada, during an 19-beam (38 beams total) experiment running from 20th to 23rd May 2019. The electron density at 250 km from a shorter time segment (x-axis) of these measurements is shown here where the beams of RISR-N and RISR-C have been sorted by magnetic latitude (y-axis). As all RISR-N beams are further North than RISR-C, all measurements in the top half of the figure are from RISR-N. A difference in calibration level is clearly visible in this example. Calculating the mean at each beam of all timesteps in the period between

155 the blue vertical lines gives the Flatfield density measurement at this altitude. This is the first example presented in Section 3 and further details of this calculation are presented there.
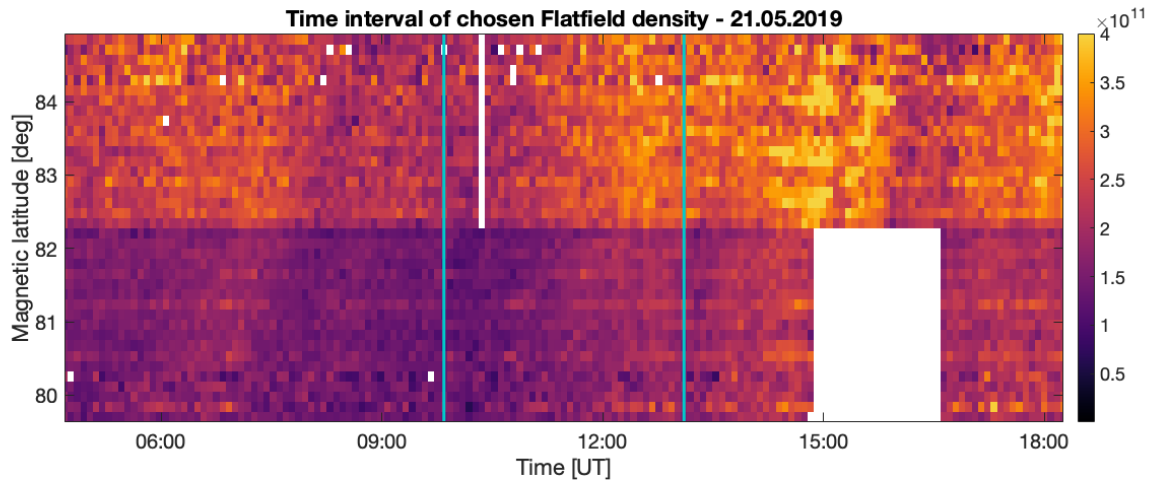
Figure 1. Electron density at 250 km measured at RISR-N (upper half) and RISR-C (lower half) during a 19-beam (38 total) experiment on 20. - 23. May 2019. Blue vertical lines indicate the chosen Flatfield density period on 21. May 2019 from 09:50 - 13:05 UT. The mean of these measurements at each beam will provide the Flatfield density measurement for the Flatfield calibration.

Using the same approach as for the Flatfield density measurements we can attempt to estimate the Darkfield density, N_e^{Df}, from the data, if and only if there is a period in the data where there were no density enhancements. This was tested for several

160 altitudes and time periods in the examples shown in this paper. However, the inclusion of a calculated Darkfield density did not appear to improve the results and for one example there were no periods without structured density enhancements. This also introduces another step and another source of uncertainty and therefore we do not have a good empirically estimated Darkfield density to include in this method. In theory, if there is no leakage of receiver noise of the ISR into the estimate of received power, then the Darkfield density value should be zero. A few different approaches were examined but a lower

165 threshold electron density of $N_e^{Df} = \overline{N_e^{Df}} = 1 \times 10^9 \, \text{m}^3$ was chosen as a suitable Darkfield density value. This corresponds to the approximate lowest density that the ISR can measure. This Darkfield density is used for all calculations using the Flatfield

correction presented in this paper. With N_e^{Ff} and N_e^{Df} estimated we can use Equation 5 and calculate a correction factor G_{FFC} for each beam at every altitude of interest. Figure 2 shows an example of correction factors calculated for all beams at eight different altitudes and Flatfield density periods, for the same experiment as in Figure 1. The green line corresponds

170   to the correction factors calculated from the Flatfield period indicated in Figure 1. Here each line shows the correction factors (y-axis) calculated for each beam (x-axis), for a horizontal altitude slice, and from a "Flatfield density period" indicated in the legend. The bold black line and shaded gray area indicate the mean and standard deviation of the correction factors. The beam numbers are assigned by simply counting the entries in the datafiles. So for this example, RISR-N beams are numbered 1 - 19 and RISR-C beams are numbered 20 - 38. It should be noted that the AMISR beam numbers presented here correspond only

175   to this specific experiment and were assigned here to aid in discussion only. The actual look direction of a given beam number may change from experiment to experiment. While each of the nearly 4000 beams for each of RISR-C and RISR-N has a fixed number which are used by the radar operators, they are typically not meaningful for discussing individual experiments. For each experiment, the actual look directions of a given beam are available in the corresponding data files.
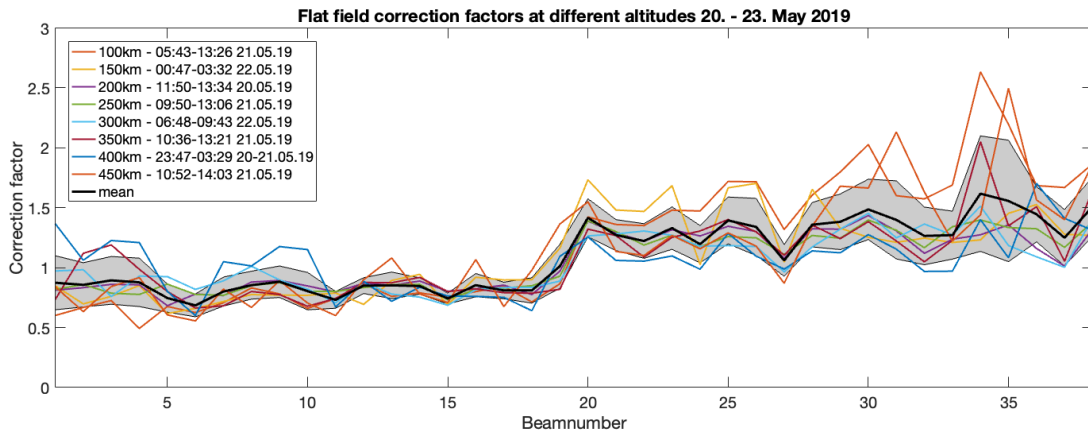
Figure 2. Correction factors, G_{FFC}, calculated from Equation 5 for Flatfield correction of the electron density measured at RISR-N and RISR-C on May 20th - 23rd 2019, during a 19-beam (38 total) experiment. Each line indicates G_{FFC} for an altitude slice through all beams with the corresponding Flatfield density period indicated in the legend. The bold black line and shaded gray area indicate the mean and standard deviation. Beam number 1-19 indicate RISR-N beams while beam umber 20-38 indicate RISR-C beams.

2.2   Ratio distribution correction of multi-point ISR data

180   A second, robust method requiring less manual input, to determine a correction factor is presented here. We calculate a ratio of electron density measurements and use the distribution of ratios to find the optimal correction factor, G_{RDC}. The ratio is given by

$$N_e^{ratio} = \frac{\overline{N_e^t}}{N_e^{beam}} \qquad (6)$$
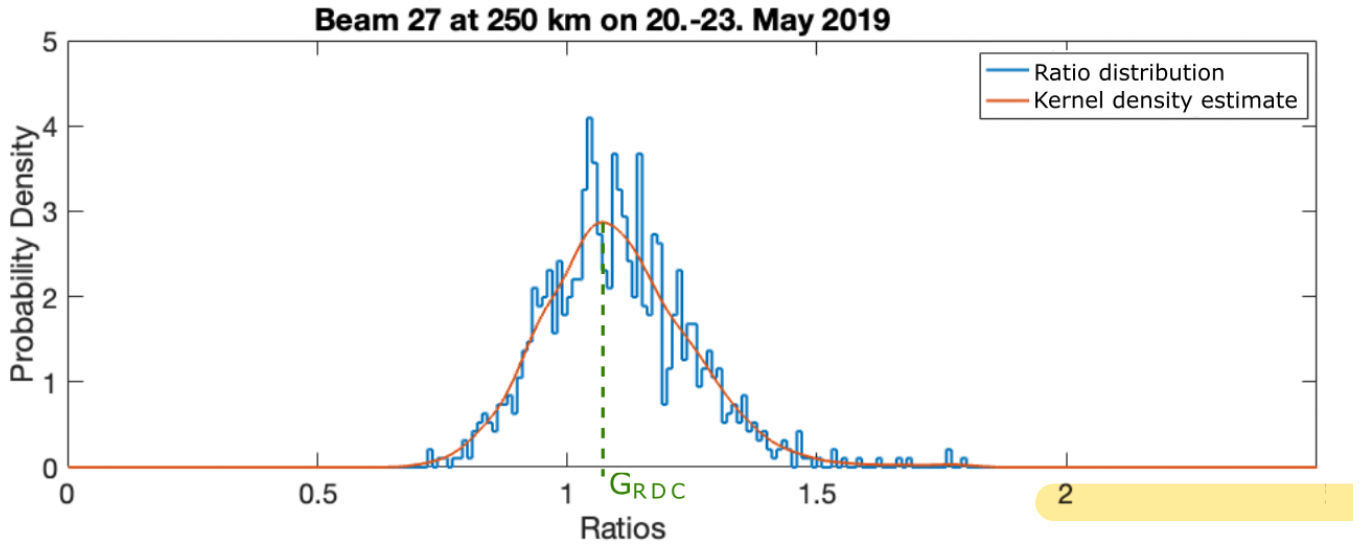
Figure 3. Kernel density estimate of the ratios between the mean of all beams at time t, and the electron density at all timesteps in beam 27 at 250 km altitude during an experiment on 20th - 23rd May 2019. The blue line indicates the distribution of the density ratios calculated using Equation 6. The red line shows the calculated Kernel density estimate of these ratios. The ratio, G_{RDC}, indicated by the green line, corresponds to the peak of the Kernel density estimate and is used as the new correction factor.

where $\overline{N_e^t}$ is the mean electron density of all beams at a timestep t ([1 × number-of-beams] - array), while N_e^{beam} is all electron density measurements at all timesteps of an experiment in a particular beam ([1×number-of-timesteps] - array). The N_e^{ratio} thus gives the ratios of the mean electron density measurement in all beams, at each time and altitude, to the electron density measurement in one beam. For every beam this gives one N_e^{ratio} for every timestep of the experiment ([1×number-of-timesteps] - array for every beam). Hence, we obtain a distribution of the ratios for each beam. We then make a Kernel density estimate of the distribution of these ratios for each beam. An example of this is shown in Figure 3. Here a histogram (blue) of N_e^{ratio} for Beam 27 at 250 km during the same experiment at RISR-N and RISR-C used for Figures 1 and 2 and the example in Section3. The Kernel density estimate is shown in red. The ratio at which the maximum probability density estimate is found is taken as the correction factor, G_{RDC}, for that beam at that altitude. This calculation is then done for all beams at the altitude of interest. The correction factor is used to scale the corresponding electron density measurement, N_e^{org}, as:

$$N_e^{corr} = N_e^{org} G_{RDC} \tag{7}$$

to obtain the corrected electron density, N_e^{corr}.

An example of how the correction factors calculated using this method can vary with beam and altitude is shown for one example in Figure 4. The correction factors are calculated for 20 km horizontal, altitude slices for all beams during an 11-beam
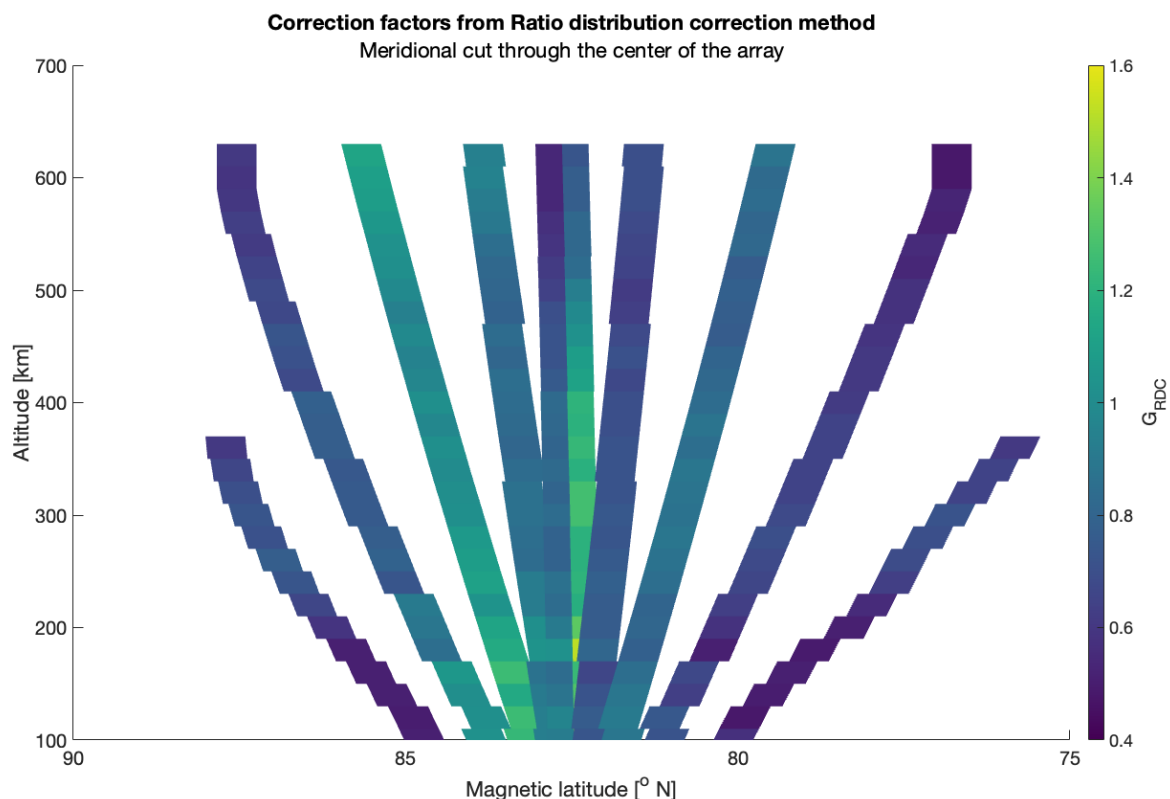
Figure 4. Calculated correction factors at all beams along the central meridian line through the arrays for the experiment running from 12th to 14th October 2016. The magnetic latitude is indicated in the x-axis and the y-axis indicates the altitudes. The correction factors are calculated using the Ratio distribution method (method 2), in horizontal 20 km thick altitude slices.

(22 total) experiment from 12th to 14th October 2016 at RISR-N and RISR-C (see the third example in Section 3). The figure
200   shows all beams along a longitudinal cut at the center meridional line of both radars. It is particularly clear from this figure that the two vertical beams from the two radars are not calibrated to match in the uncorrected electron density data as they have very different correction factors. It should be noted that this difference is also explained by the large error estimate (not shown) of these particular two beams.

3   Examples

205   The results of both methods are shown in the following three examples. The methods presented here are applicable to any multi-point radar measurement. In anticipation of the EISCAT 3D radar (McCrea et al., 2015; Kero et al., 2019), we utilize data from the AMISR phased array radar system to investigate the calibration techniques described above. Hence, we have chosen three experiments, running different radar modes with different numbers of beams from the large RISR-N and RISR-C

databases. All data shown here was downloaded from the online databases and error-filtered as suggested in the AMISR user
manual (Lamarche, 2022). That is, electron density measurements smaller or the same size as the error estimate, dNe, and
data where the data quality parameters were poor, were excluded (set to Not-a-number). The error estimate and data quality
parameters are normal data products provided for all RISR-N and RISR-C data. To show the results of the two methods, for
each example (see Figure 5, 6 and 7), we show the uncorrected electron density for all beams at one altitude in the top panel.
The beams are ordered by magnetic latitude (y-axis) so that all beams from RISR-N are in the upper half, while beams from
RISR-C are shown in the lower half of the panel. The plots show the experiments for the times (x-axis) where both radars
were running simultaneously. With careful investigation of the electron density data, we then identified a time period where
the electron density was enhanced but not structured or showed very little structure. Ideally, quiet-time daytime periods. These
periods are indicated by the vertical blue lines in the top panel. From a time average of this period, we obtain the Flatfield
density of the radar beams. Doing the Flatfield correction (method 1) as described above we obtain the Flatfield corrected
electron density, shown in the middle panel, for each example. Lastly, the bottom panel of each figure shows the result of the
Ratio distribution correction (method 2). In Figure 7, additional white lines and white shaded areas indicate the position of the
terminator at the given altitude during the experiment. Figure 5 and 6 do not have these as the ionosphere in the field of view
of the radar was continuously sunlit during these experiments.

The first example is from an *imaginglp* experiment run from 19-May-2019 22:01:09 UT to 23-May-2019 14:19:46 UT on
RISR-N and RISR-C. Figure 5 shows the uncorrected, Flatfield corrected, and Ratio distribution corrected electron densities
with a five-minute time resolution. This radar mode has 19 beams per radar (38 total), and at 250 km altitude the field of view
is from 79.927^o to 84.6578^o North in magnetic latitude. In the upper panel, a calibration difference is clearly visible. The
upper half, showing uncorrected electron density from RISR-N, is approximately 1×10^{11} m^{-3} larger than all observations
from RISR-C, during the experiment, and significant beam-to-beam variations can be seen. This calibration difference could
be problematic when analyzing the data. The two vertical blue lines in the top panel indicate the period chosen to calculate the
Flatfield density. This is the same period that is shown as a close-up in Figure 1. We calculate the correction factors from the
time-averaged mean for this period at this altitude using Equation 5. The green line in Figure 2 corresponds to the result from
that calculation. The corrected electron density, using the Flatfield correction method at this altitude is shown in the middle
panel. In the bottom panel the corrected electron density, using the Ratio distribution correction method, is shown. The small
blue arrow on the right indicates beam 27, which is used as an example to show the Ratio distribution and Kernel density
estimate in Figure 3.

The second example is from a 22 beam (44 total) *Convection67m* radar mode experiment run on RISR-N and RISR-C from
03-May-2018 15:55:25 UT to 04-May-2018 14:59:45 UT. Figure 6 shows the electron density and the results of the two correc-
tion methods from calculations at 200 km altitude with a one-minute time resolution. In the top panel, showing the uncorrected
electron density, there are nonphysical step changes between the electron densities in neighboring beams which are persis-
tent throughout the experiment. That is, these differences are apparent for both high and low electron densities. These sharp

Figure 5. Electron density at 250 km altitude from 38 beams, measured at RISR-N and RISR-C in the *imaginglp* radar mode from 19-May-2019 22:01:09 UT to 23-May-2019 14:19:46 UT. The top panel is the uncorrected, error-filtered, electron density as downloaded from the online databases. The middle panel shows the Flat field corrected electron density where the flat field is determined from the period between the two vertical blue lines in the top panel. The bottom panel shows the Ratio distribution corrected electron densities. All beams are sorted by magnetic latitude (y-axis) such that RISR-N beams appear on the top half of every panel, while RISR-C beams are on the bottom half. The small blue arrow to the right, in the bottom panel indicates beam 27 used as an example in Figure 3.

transitions are likely caused by some calibration issue, as they are consistent throughout the dataset. Both correction methods
245   improve the electron density data and the instrumental effects of the density differences are reduced. After this calibration, the
density structures moving through the field of view of the radars are still clearly visible.

The *Worldday66* beam mode ran on RISR-N and RISR-C from 12-Oct-2016 21:27:07 UT to 15-Oct-2016 13:59:26 and
12-Oct-2016 21:41:27 UT to 14-Oct-2016 22:05:22 UT, respectively. Figure 7 shows the measured electron density at 200 km
250   altitude from this experiment with a one-minute time resolution. This radar mode has 11 beams, so simultaneous observations
with RISR-N and RISR-C give 22 beams in total with a field of view spanning from 75.5860N to 87.7 degrees North magnetic
latitude at 200 km altitude. In this figure, a difference in calibration is apparent, as RISR-C (bottom half) appears to consistently
observe higher electron densities than RISR-N in the top panel. To separate this difference from a possible difference in
illumination and thus ionization, the white lines in all panels indicate the position of the shadow terminator at this altitude. The
255   shaded area is where the ionosphere at this altitude is in darkness. Additionally, it should be noted that three beams (beams
1,12,22 counting from the top) seem to differ significantly from the other beams in the radar. From the error of the fitted
electron density, dNe (data product from AMISR, not shown), it is clear that those three beams also show the largest mean
errors.

4   Quality and error estimates

260   The robustness and uncertainties of our methods are investigated separately. In principle, the presented methods are similar
to the process performed before the data is made publicly available, in that a *Magic constant* or *system constant* is used to
scale the measurements to calibrate for known characteristics of a given radar. The two presented methods however calculate a
correction factor from the electron density measurements itself. Thus, we assess the ability of the methods to provide a relative
correction. Two different approaches are used for the two methods.

265

For the Flatfield correction (method 1), we meticulously choose the Flatfield density periods at each altitude and inspect the
resulting corrected electron densities. Given that the corrected electron densities appear plausible, improved, and no obvious
eccentricities are detected, we consider the calculated correction factor as good. Comparing the correction factors from different periods and altitudes and calculating the mean and standard deviation of these gives an impression of how variable the
270   results of these calculations are. Figure 2 shows this for the first example (see Figure 7). Here the mean and standard deviation
from eight altitudes and Flatfield density periods are shown by the bold black line and grey-shaded area, respectively. One
might consider it reasonable to calculate the mean of these correction factors from all altitudes and use them as a correction
factor for whole beams, independent of altitude. However, as a given altitude will be at different ranges for different beams
and the apparent antenna gain varies with range and pointing direction, it would impact the results negatively. This was tested
275   by the authors and the improvements were significantly diminished. This can also be understood from Figure 4, showing the
correction factors calculated in 20 km horizontal altitude slices, in beams along a longitudinal, magnetic meridian. Although
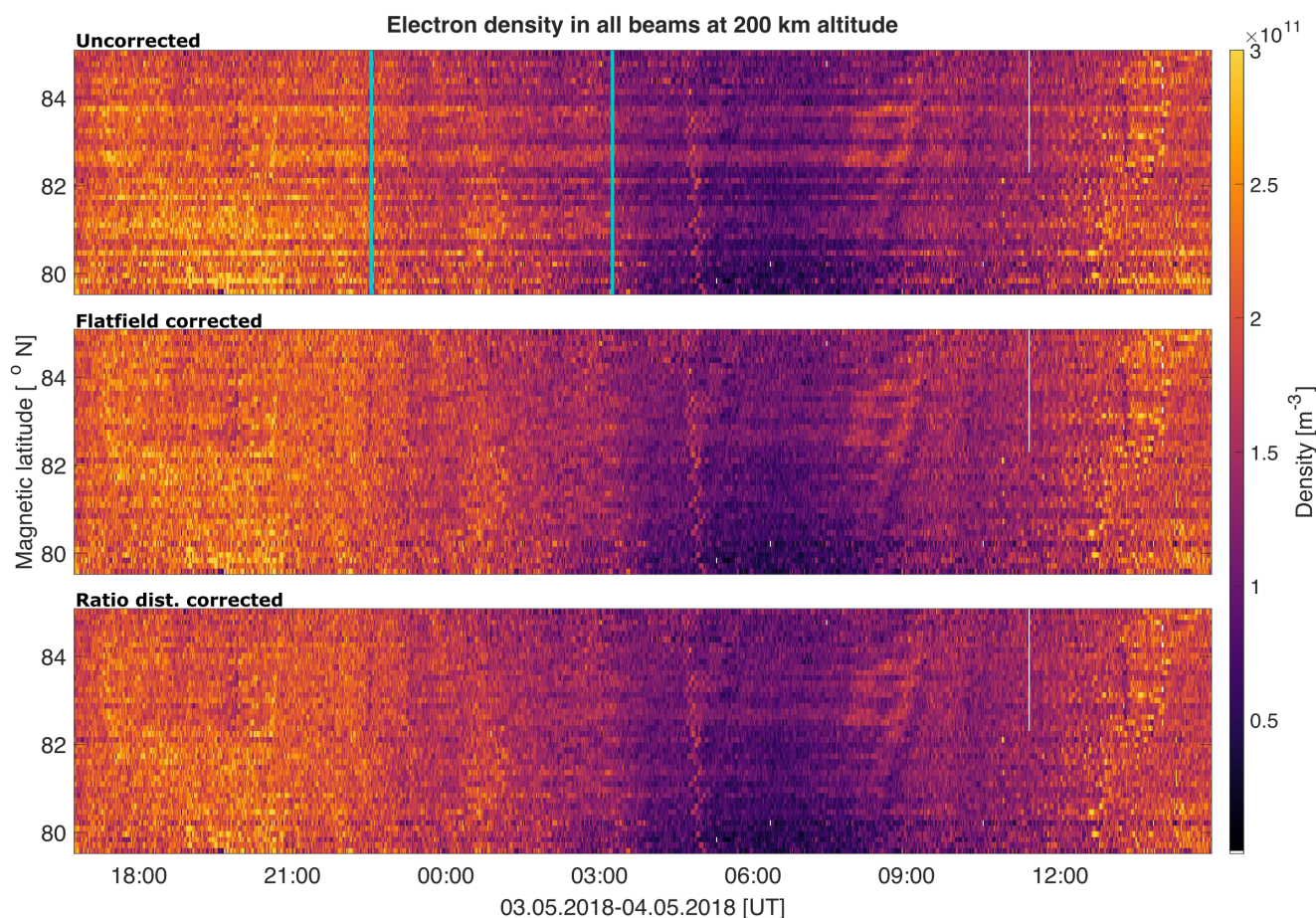
Figure 6. Electron density at 200 km altitude from 44 beams, measured at RISR-N and RISR-C in the *Convection67m* radar mode, from 03-May-2018 15:55:25 UT to 04-May-2018 14:59:45 UT. The Figure is in the same format as Figure 5.

the second method is used for the calculations here, we expect both methods to give comparable results and we see here that the correction factors vary slightly with altitude within the separate beams.

280 To assess the quality and robustness of the Ratio distribution correction (method 2) we present two approaches. In the first, we divide the uncorrected data from one experiment into smaller subsets of the whole experiment period. We then redo the calculations using the same method and compare the results to the results from using the whole dataset. Since we calculate the correction factor for every altitude and beam from the maximum of the distribution of N_e^{ratio} for every beam, outliers, and enhancement, as well as very low measurements are effectively removed from the calculations. In Figure 3 this can be observed

285 as we see a wide range of N_e^{ratio} measured within the same experiment. By taking smaller subsets of the whole dataset and
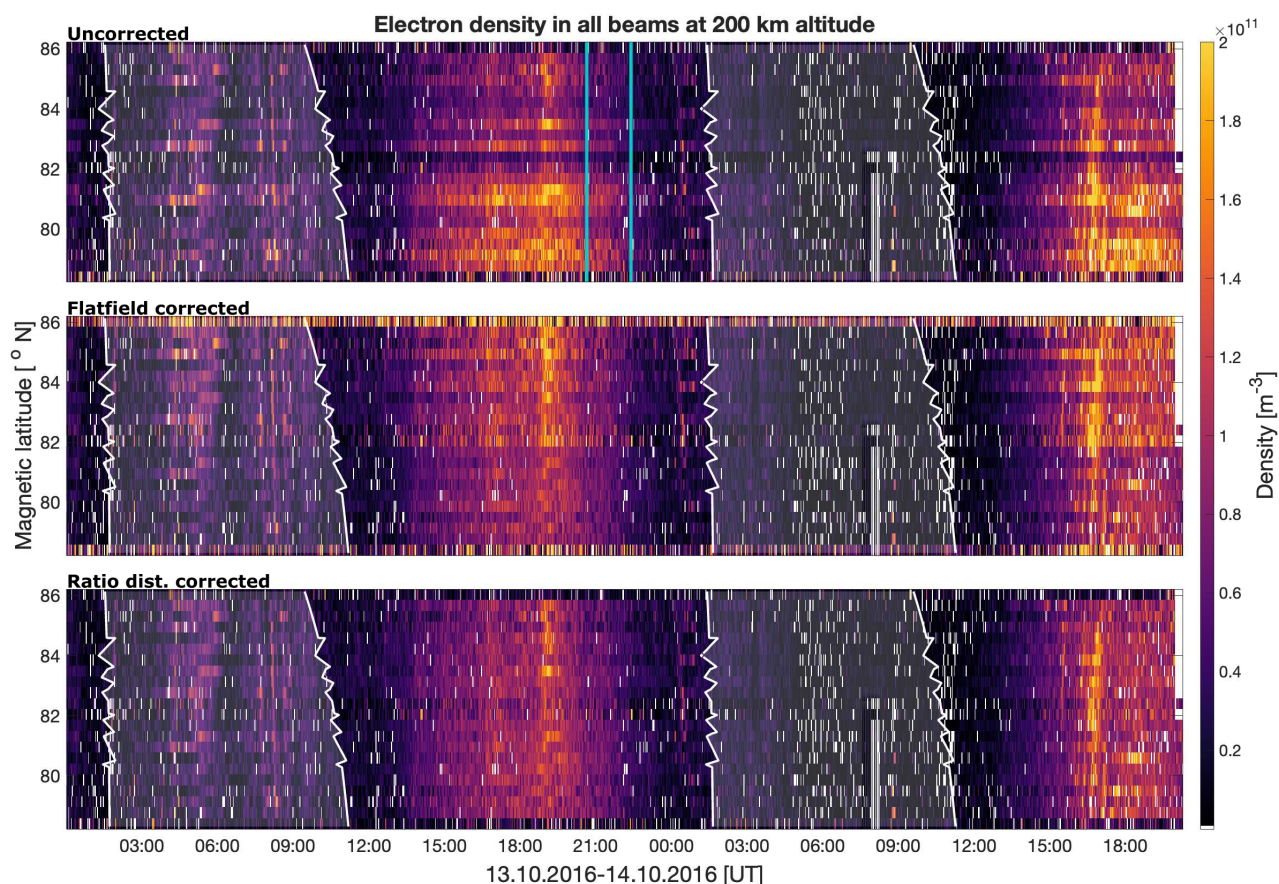
Figure 7. Electron density at 200 km altitude, measured at RISR-N and RISR-C from 12-Oct-2016 21:27:07 UT to 15-Oct-2016 13:59:26. The FIgure is in the same format as Figure 5 and 6. This Figure also shows the position of the terminator/shadow at this altitude, indicated by the white lines. The gray shaded regions in all panels indicate when the ionosphere is in darkness (shaded).

comparing the results, an estimate is obtained of how well the filtering of outliers and enhancements performs. This is because one might get subsets only containing enhanced values or a very structured subset including multiple polar cap patches or similar auroral events. It also gives an indication of how robust the method is with regard to the length of a dataset and thus, the number of N_e^{ratio} measurements needed for a good result. Figure 8 shows the corrected electron densities from the data pre-
290 sented in Figure 5 when using subsets of 24 hours, 12 hours, 6 hours, and 1 hour. It is clear from this Figure that more "lines" or sharp transitions between beams (beams that appear to be differently calibrated from the rest) appear when using successively smaller subsets of data. The corrected electron densities get progressively worse when reducing the number of measurements used for the calculation. This is expected as a reasonable number of measurements are necessary to achieve a representative distribution of N_e^{ratio}, to estimate the probability density and to find its maximum value. To quantify this quality of the result
295 we have recalculated the correction factor using 1000 randomly selected subsets of data and calculated the standard deviation and variance of $G_{(}RDC)$. This is shown in Figure 9 where the green and purple shaded areas indicate the standard deviation and variance, respectively. The mean of the correction factor at each beam for every subset will converge toward the correction factor as calculated from the full dataset. This is because running many iterations of a randomly chosen one-hour subset of data will eventually cover the full experiment dataset and so the mean of all iterations will be the same as calculating the correction
300 factors once from the full dataset. However, the standard deviation and variance indicate how sensitive the correction factor calculations are to the size of a subset of data compared to the full dataset.

The second approach used to assess the robustness of the Ratio distribution correction method is by fitting a Gaussian function to the Kernel density estimate of the distribution of N_e^{ratio}. The density function from the Kernel density estimate is not
305 expected to resemble a Gaussian function as a whole, as electron density data generally contains data from transient events like polar cap patches, auroral events, or precipitation events that are not expected to be normally distributed throughout an experiment. The N_e^{ratio} corresponding to the peak probability density indicates the most common ratio for the given beam at the given altitude for the current experiment. By fitting a Gaussian function to the Kernel density estimate in close proximity to this maximum, we can calculate the width of the Gaussian. This is used as a measure of the standard deviation of the N_e^{ratio}
310 distribution and leads us to an estimate of the uncertainty of the correction factor. Additionally, the standard error of the mean can be calculated. The mean is the shift of the Gaussian distribution, which corresponds to the N_e^{ratio} value at which the peak of the probability density occurs. This is done for the three examples presented above in Figures 5, 6 and 7. Figure 10 shows the calculated correction factors (y-axis) using the Ratio distribution correction method at the respective altitudes as presented in the Figures above. The standard deviation and standard error of the mean of the fitted Gaussian function are indicated for
315 each beam (x-axis), by the yellow and orange bars, respectively.

5   Discussion

We present two methods to improve the calibration of multi-beam ISR electron density data. The methods are fundamentally the same as both calculate correction factors, G, that are subsequently used to scale the electron density measurements. It is
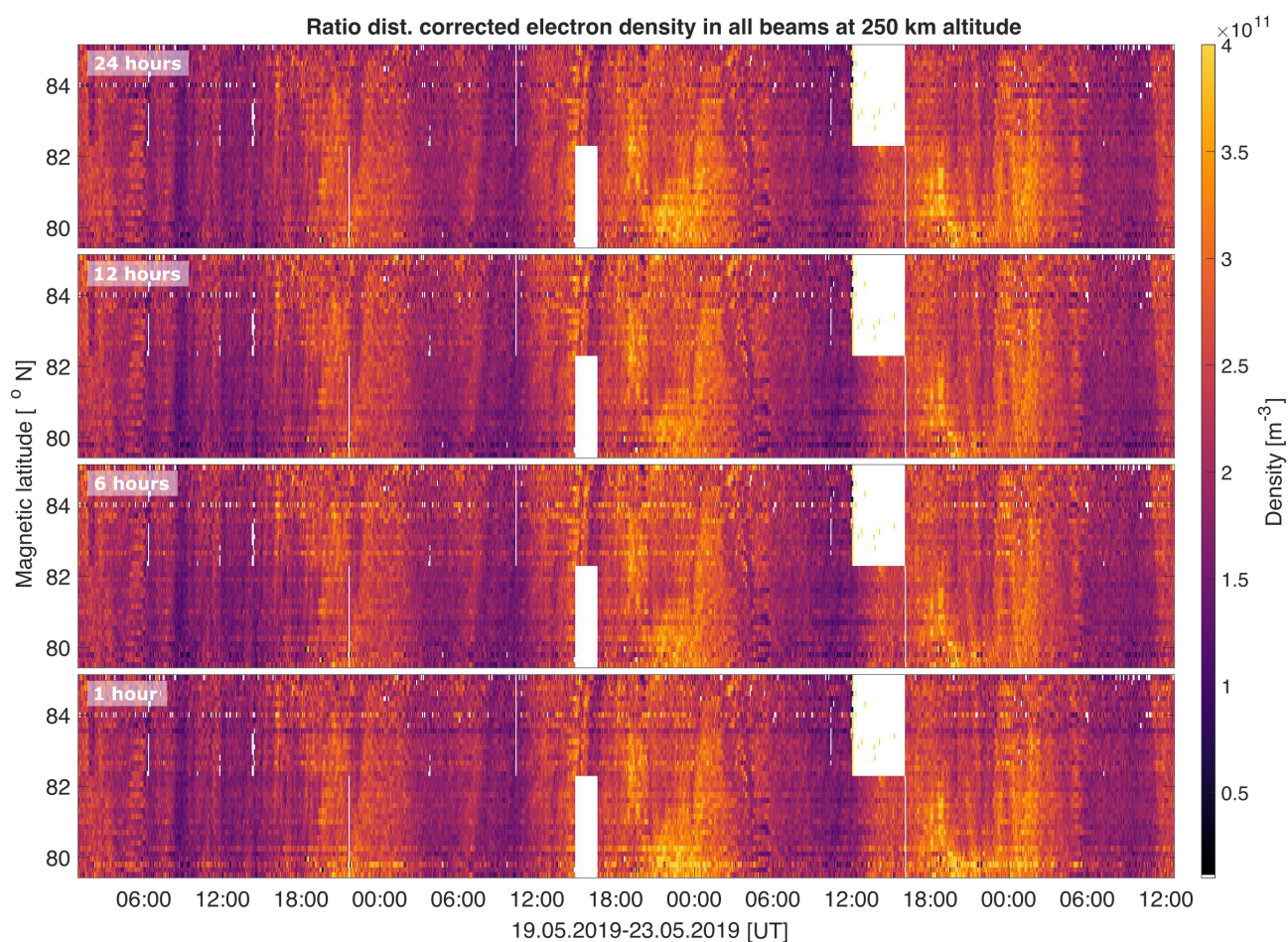
Figure 8. Corrected electron density at 250 km altitude from 38 beams during the experiment presented in example 3, Figure 5. In each panel, a randomly chosen subset of the full dataset from the experiment was used to calculate the correction factor from the ratio distribution of the electron density ratios (Method 2). The top panel shows the result for using a 24-hour subset of data, the second for twelve hours, and the two bottom panels show the result for a six and one-hour subset of data. The subsets are chosen randomly from the 3.5-day dataset.
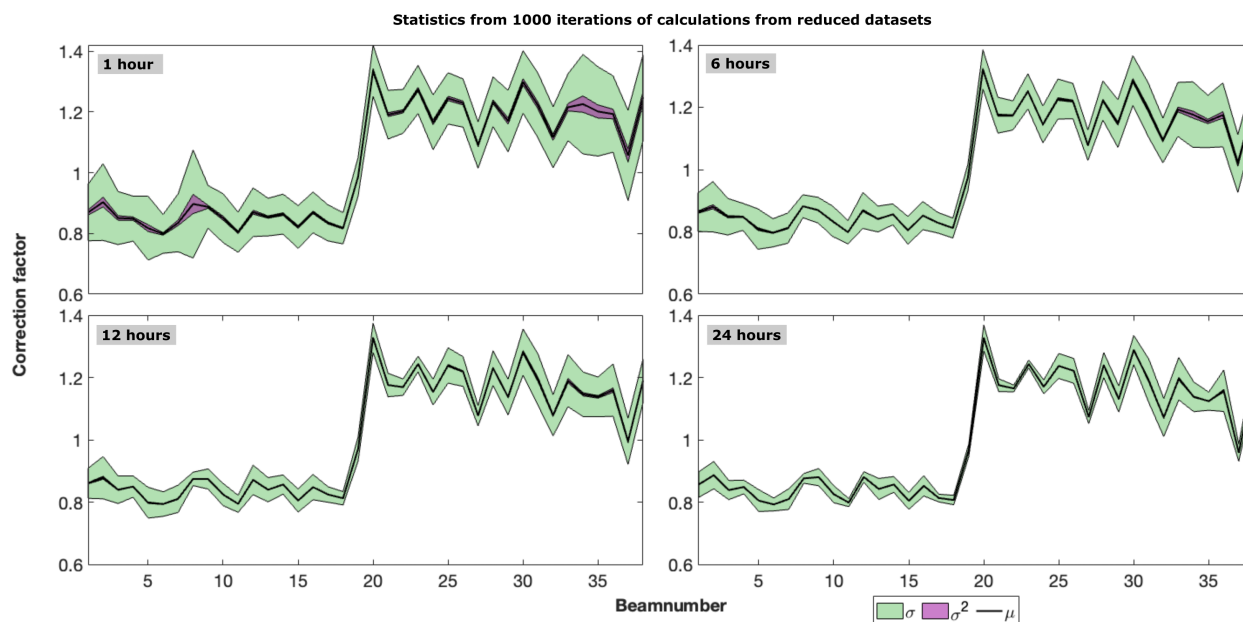
Figure 9. The standard deviation and variance of the calculated correction factors when using subsets of a larger dataset. The calculations for the correction factor are repeated 1000 times using a 1-, 6-, 12-, and 24-hour, randomly chosen subset of data. The standard deviation and variance of these iterations are indicated by the green and purple shaded areas respectively. The black line indicates the mean of the iterations and will converge to the same values as for calculations done once using the full dataset.

similar to the adjustments of the *magic constant* and *system constant* used by the EISCAT and AMISR radars, respectively
320 (see Equation 4). The *magic constant* and *system constant* are inferred from knowledge of the radar system and the characteristics of the antenna pattern and radar parameters used for a given experiment. In contrast, the correction factors obtained from the two methods described here are determined from the multi-beam electron density data itself. Thus, our proposed methods do not attempt to replace current calibration methods but rather add a second-level calibration correcting for variable, unpredictable, and unaccounted variations in system gain. As such this procedure should be considered as an integral part of
325 the data-processing chain for every multi-beam ISR.

Both methods are based on the established Flat field calibration method used in imaging and photography (see for example Burke, 1996, and references therein.). In method 1 the user manually selects a suitable Flatfield density (or reference), considering our knowledge of the underlying physics, to find G. Method 2 uses a statistical approach, considering the distribution of
330 the measurements, to estimate G. Here, the distribution of electron density ratios for each beam are found. Through a Kernel density estimate, we obtain the estimated correction factor which is used to obtain corrected electron density measurements.

In the case of good/ideal basic (first-level) calibration, these methods scale all electron densities with a factor of $G = 1$ in each beam. If there are unaccounted variations these methods contribute to a near ideal calibration. Additionally, for the case
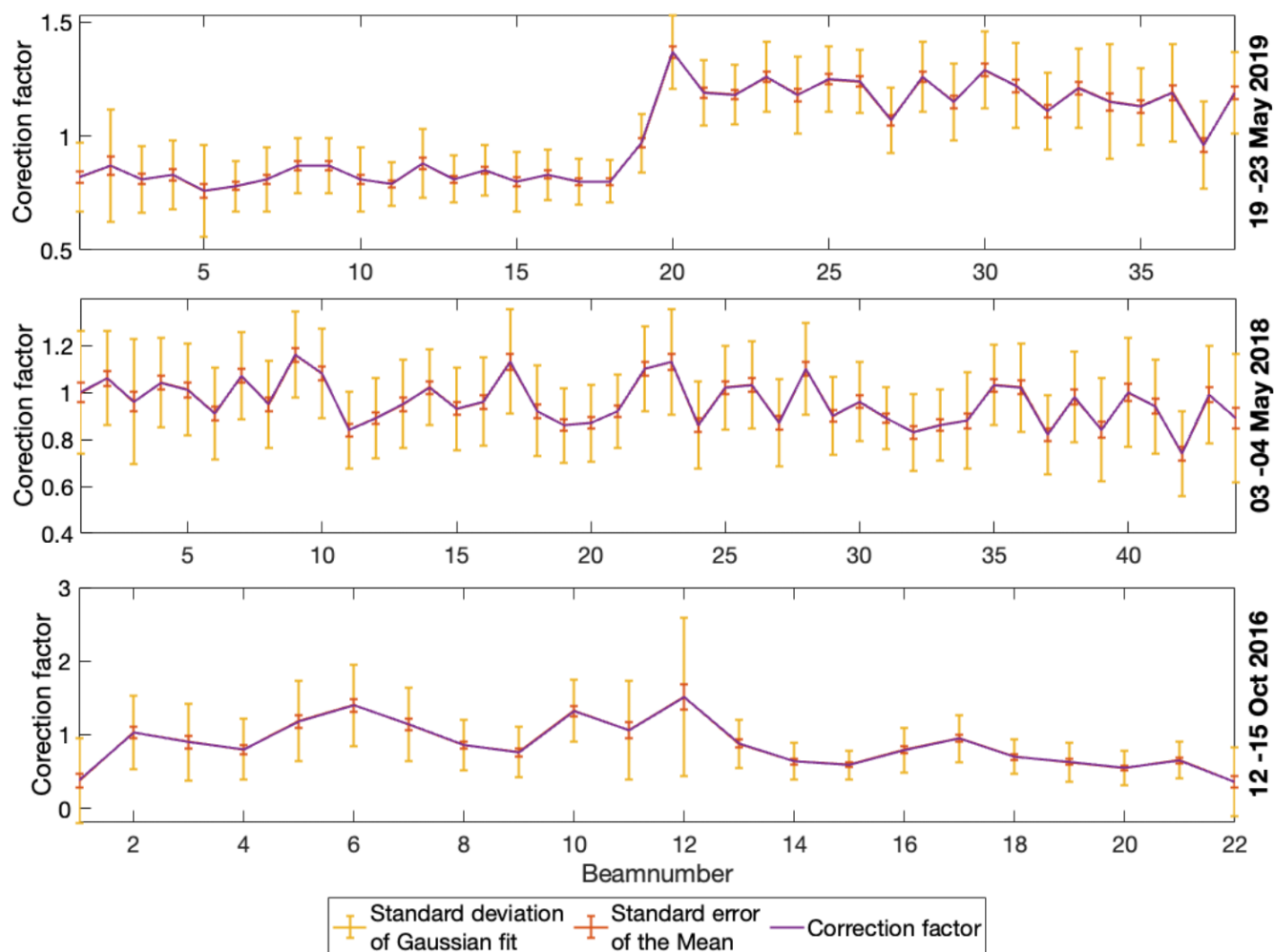
Figure 10. The standard deviation and standard error of the mean of the fitted Gaussian distribution to the ratio distributions giving the correction factors, for the three experiments presented as examples in Figure 5, 6 and 7. These are calculated at 250, 200, and 200 km altitude at all beams respectively, corresponding to the altitudes shown in the examples.

where the electron density in one beam is accurately calibrated, for example with a plasmaline measurement, all calibration

335 factors then should be scaled such that the calibration factor of that beam is $G = 1$. Lacking a beam with such accurate calibration, there will be one system-wide calibration scaling uncertainty. The calibration methods presented here are useful also for future experiments and future radars like EISCAT 3D, where data volume is an issue, as it would reduce the need for a plasmaline measurement in every beam.

340 One notable result of our methods is observed in Figure 4 where it is clear that different correction factors are needed for different ranges within the same beam. The received signal power in the radar should decrease by a factor of $\frac{1}{R^2}$ with range, only, and this factor is taken into account when estimating electron density. However, there are several effects that might result in an additional factor in an apparent range dependency of the *magic constant* (antenna gain change over range) that could account for this. A positive bias effect might occur at ranges and for experiments where a very low electron density is measured. This can

345 occur in the analyses of the raw backscattered signal, but it likely also develops when we filter the electron density by the error estimate dN_e, provided in the datafiles. Values of electron density that are lower or the same magnitude as the error estimate are discarded, leading to a positive bias in the estimate of electron density in regions and at ranges where electron density is lower (e.g. long-range or E-region during quiet-time conditions). A similar positive bias effect could occur if the measurement error distribution is asymmetric due to a non-zero constraint in the fit of the plasma parameters in the signal analyses. Another

350 reason for an altitude-dependent correction factor is leakage of system noise into the zero-lag estimate of the ionospheric echo power, which may occur due to e.g., the receiver impulse response causing receiver noise to contaminate also longer lags of the autocorrelation function estimates. Further, radio interference on the backscattered signal may also introduce additional errors that differ at different ranges. It is possible that a better estimate of the Darkfield in method 1, and the inclusion of a Darkfield in method 2 would remove the apparent difference gain with range. However, our study showed that the method in which this

355 Darkfield is acquired would have to be different from the Flatfield density acquisition described in Section 2. A potentially better option might be to estimate the above-mentioned biases and system-noise leakage and include in a Darkfield, possibly from the error measurement distribution. This Darkfield would account for the range dependency of the gain observed in our data. Due to variations in for example snow coverage, antenna elements failing, operating temperature ground conditions, etc. the Darkfield should ideally be calculated separately for every experiment. The calculation and consideration on the best method

360 to acquire a Darkfield are suggested as the next step for this study.

In Section 3 it was shown that there is sometimes a need to compensate for irregularities and nonphysical step-changes in the calibration of multi-beam electron density data from ISRs. Additionally, there is no way to determine which radar beam is the "correct" one without a separate, independent measurement. The presented examples show that both methods improve

365 calibration and data useability. This is especially valuable for research where quantitative, inter-beam comparisons of electron density changes are of interest, for example, studies of plasma patches, irregularities, and turbulence. Although there is a general need for accurate independent measurements for optimal calibration, we argue that by applying one of the methods,

the electron density measurements in all pointing directions within one experiment become inter-calibrated. An effort was made to analyze the quality and robustness of both methods in Section 4.

370 A challenge specific to the Ratio distribution correction method is considered in Figure 9. Although the Ratio distribution method can efficiently be applied to any multi-beam ISR experiment, it is somewhat sensitive to the length of the dataset. That is, to acquire a good Kernel density estimate of the ratio distribution, an adequate number of measurements are required. Figure 9 illustrates this as it is clear that the results of the correction become progressively worse when reducing the number of measurements. This means that there is a minimum number of measurements needed to acquire a reasonable result. The

375 required number of measurements changes depending on the experiment and data resolution. However, the result illustrated in Figure 9 indicates that a 12-hour experiment duration produces a noticeable improvement in the RISR experiment used as an example.

A challenge specific to the Flatfield correction method arises from the determination of a suitable Flatfield density period. Identifying a period in the electron density measurements where a uniform enhancement of electron densities is observed

380 but no polar cap patches, precipitation, or other enhancements that cause clear structuring requires manual work and can be time-consuming and difficult. However, as demonstrated in the second example, presented in Figure 6, the method can still be effective. Here we can see a slight density enhancement between 00:00 and 02:00 UT on 3rd May 2018, around 80-83°N in magnetic latitude. This enhancement is included in the identified Flatfield density period. However, the result of the Flatfield correction, shown in the middle panel, appears to be good and comparable to the results of the Ratio distribution correction

385 method. In addition to being time-consuming, due to the need to manually determine a suitable Flatfield density period, this method also appears to be slightly less proficient than the Ratio distribution method from the three examples presented in this paper.

6 Conclusions

Calibration of ISR is a complex and difficult task, especially when independent measurements of the electron density are

390 only available in one pointing direction or not at all. We have proposed two methods for the correction of electron density measurements from multi-point ISRs. These add to the current efforts that are made for the calibration of multi-point radars and can increase data usability and quality by considering variable, unaccounted and, unpredictable variations in system gain. Both methods are based on the well-established Flatfield correction method in imaging and photography. We exploit the analogy between independent measurements in separate pixels in one image sensor and multi-beam radar measurements. Based on our

395 understanding of the underlying physics and processes in the ionosphere, a suitable Flatfield is found and used to calculate a correction factor. In the second method, the correction factors are estimated, based on a Kernel density estimate of the distribution of N_e^{ratio} calculated from all measurements of an experiment. This is subsequently used to estimate the correction factor. The ratio distribution method is robust and efficient, yielding slightly better results than the Flatfield method for the examples presented here. It is sensitive to the length of the experiments when these are well below 12 hours. The errors and

400 robustness of the methods were estimated through three different approaches, one for the Flatfield correction and two for the

Ratio distribution correction. Accurate independent measurements are needed to determine absolute values of electron density and an optimal calibration. However, we argue that by applying one of the methods, the electron density measurements in all pointing directions within one experiment become inter-calibrated. Thus this second-level calibration is especially valuable for studies of plasma patches, irregularities, turbulence, and other research where inter-beam changes of electron density are of

405 interest.

Both methods are strictly based on the observed electron density data and require no additional input. They are efficient and their application on existing and future data is straightforward. Method 2 specifically requires minimal user input and is not expected to increase the demand for computing power. Thus, we suggest that these methods be implemented and applied as a second-level calibration in future calibration schemes of multi-point radars where any calibration is required. This will improve

410 the calibration and data accuracy of phased array incoherent scatter radar measurements and thus overall data useability and quality.

Data availability. All RISR-N data used in this study are available from the SRI database at https://data.amisr.com/database/, while RISR-C data can be downloaded at https://www.ucalgary.ca/aurora/projects/risrc. All data can also be downloaded from Madrigal at https://isr.sri.com/madrigal/.

415 *Author contributions.* Conceptualization: TR, BG; Methodology: TR, BG; Writing: TR, JV; Discussion: all; Reading and Reviewing; all

Competing interests. No competing interests are present.

Acknowledgements. RISR-C is funded by the Canada Foundation for Innovation and led by the University of Calgary's Auroral Imaging Group, in partnership with UofC Geomatic Engineering, University of Saskatchewan, Athabasca University and SRI International and the authors would like to thank all parties for making data available. Our thanks is also given to the SRI International team for making available

420 data from the RISR-N radar. Further, the authors would like to thank the Research Council of Norway grant (CASCADE 326039). DH was funded during this study through a UiT The Arctic University of Norway contribution to the EISCAT 3D project funded by the Research Council of Norway through research infrastructure grant 245683.

References

Bahcivan, H., Tsunoda, R., Nicolls, M., and Heinselman, C.: Initial ionospheric observations made by the new Resolute incoherent scatter radar and comparison to solar wind IMF, Geophysical Research Letters, 37, https://doi.org/10.1029/2010GL043632, 2010.

Baumjohann, W. and Treumann, R.: Basic Space Plasma Physics, Imperial College Press, revised edn., 2012.

Bibl, K.: Evolution of the Ionosonde, ANNALI DI GEOFISICA, 41, 1998.

Burke, M. W.: Image Acquisition, Springer Netherlands, https://doi.org/10.1007/978-94-009-0069-1, 1996.

Evans, J. V.: Theory and practice of ionosphere study by Thomson scatter radar, Proceedings of the IEEE, 57, 496–530, 1969.

Fejer, B. and Kelley, C.: Ionospheric Irregularities, Reviews of geophysics and space physics, 18, 401–454, 1980.

Forsythe, V. V. and Makarevich, R. A.: Statistical Analysis of the Electron Density Gradients in the Polar Cap F Region Using the Resolute Bay Incoherent Scatter Radar North, Journal of Geophysical Research: Space Physics, 123, 4066–4079, https://doi.org/https://doi.org/10.1029/2017JA025156, 2018.

Gillies, R. G., van Eyken, A., Spanswick, E., Nicolls, M., Kelly, J., Greffen, M., Knudsen, D., Connors, M., Schutzer, M., Valentic, T., Malone, M., Buonocore, J., St.-Maurice, J. P., and Donovan, E.: First observations from the RISR-C incoherent scatter radar, Radio Science, 51, 1645–1659, https://doi.org/10.1002/2016RS006062, 2016.

Gillies, R. G., Perry, G. W., Koustov, A. V., Varney, R. H., Reimer, A. S., Spanswick, E., St.-Maurice, J. P., and Donovan, E.: Large-Scale Comparison of Polar Cap Ionospheric Velocities Measured by RISR-C, RISR-N, and SuperDARN, Radio Science, 53, 624–639, https://doi.org/10.1029/2017RS006435, 2018.

Goodwin, L. V. and Perry, G. W.: Resolving the High-Latitude Ionospheric Irregularity Spectra Using Multi-Point Incoherent Scatter Radar Measurements, Radio Science, 57, https://doi.org/10.1029/2022RS007475, 2022.

Kelly, J. and Heinselman, C.: Initial results from Poker Flat Incoherent Scatter Radar (PFISR), Journal of Atmospheric and Solar-Terrestrial Physics, 71, 635, https://doi.org/https://doi.org/10.1016/j.jastp.2009.01.009, advances in high latitude upper atmospheric science with the Poker Flat Incoherent Scatter Radar (PFISR), 2009.

Kero, J., Kastinen, D., Vierinen, J., Grydeland, T., Heinselman, C., Markkanen, J., and Tjulin, A.: EISCAT 3D: THE NEXT GENERATION INTERNATIONAL ATMOSPHERE AND GEOSPACE RESEARCH RADAR, ESA Space Safety Programme Office, www.space-track.org, 2019.

Kintner, P. M. and Seyler, C. E.: The status of observations and theory of high latitude ionospheric and magnetospheric plasma turbulence, Space Science Reviews, 41, 91–129, https://doi.org/10.1007/BF00241347, 1985.

Lamarche, L.: AMISR User Manual, https://ljlamarche.github.io/amisr_user_manual/intro.html, 2022.

Lamarche, L. J. and Makarevich, R. A.: Radar observations of density gradients, electric fields, and plasma irregularities near polar cap patches in the context of the gradient-drift instability, Journal of Geophysical Research: Space Physics, 122, 3721–3736, https://doi.org/https://doi.org/10.1002/2016JA023702, 2017.

Lamarche, L. J., Varney, R. H., and Siefring, C. L.: Analysis of Plasma Irregularities on a Range of Scintillation-Scales Using the Resolute Bay Incoherent Scatter Radars, Journal of Geophysical Research: Space Physics, 125, https://doi.org/10.1029/2019JA027112, 2020.

McCrea, I., Aikio, A., Alfonsi, L., Belova, E., Buchert, S., Clilverd, M., Engler, N., Gustavsson, B., Heinselman, C., Kero, J., Kosch, M., Lamy, H., Leyser, T., Ogawa, Y., Oksavik, K., Pellinen-Wannberg, A., Pitout, F., Rapp, M., Stanislawska, I., and Vierinen, J.: The science case for the EISCAT 3D radar, vol. 2, Progress in Earth and Planetary Science, https://doi.org/10.1186/s40645-015-0051-8, 2015.

Montgomery, S. D., Drake, R. P., Jones, B. A., and Wiedwald, J. O.: Flat-field response and geometrlc distortion measurements of optical
460   streak cameras, High Speed Photography, Videography, and Photonics V, 0832, 283–288, https://doi.org/10.1117/12.942241, 1988.

Oswalt, T. D. and Bond, H. E.: Planets, Stars and Stellar Systems: Astronomical Techniques, Software, and Data, vol. 2, Springer Dordrecht,
https://doi.org/10.1007/978-94-007-5618-2, 2013.

Rexer, T., Gustavsson, B., Leyser, T., Rietveld, M., Yeoman, T., and Grydeland, T.: First Observations of Recurring HF-
Enhanced Topside Ion Line Spectra Near the Fourth Gyroharmonic, Journal of Geophysical Research, Space Physics, 123, 1–15,
465   https://doi.org/10.1029/2018JA025822, 2018.

Semeter, J., Butler, T., Heinselman, C., Nicolls, M., Kelly, J., and Hampton, D.: Volumetric imaging of the au-
roral ionosphere: Initial results from PFISR, Journal of Atmospheric and Solar-Terrestrial Physics, 71, 738–743,
https://doi.org/https://doi.org/10.1016/j.jastp.2008.08.014, advances in high latitude upper atmospheric science with the Poker Flat
Incoherent Scatter Radar (PFISR), 2009.

470   Themens, D. R., Jayachandran, P. T., Nicolls, M. J., and MacDougall, J. W.: A top to bottom evaluation of IRI 2007 within the polar cap,
Journal of Geophysical Research: Space Physics, 119, 6689–6703, https://doi.org/https://doi.org/10.1002/2014JA020052, 2014.

Tsinober, A.: An Informal Conceptual Introduction to Turbulence, https://doi.org/10.1007/978-90-481-3174-7, 2009.

Tsunoda, R. T.: High-latitude F region irregularities: A review and synthesis, Reviews of Geophysics, 26, 719–760,
https://doi.org/https://doi.org/10.1029/RG026i004p00719, 1988.